

# Kink-Antikink Interaction Forces and Bound States in a $\phi^4$ Model with Quadratic and Quartic dispersion

G. A. Tsolias,<sup>1</sup> Robert J. Decker,<sup>2</sup> A. Demirkaya,<sup>2</sup> T.J. Alexander,<sup>3</sup> and P. G. Kevrekidis<sup>1</sup>

<sup>1</sup>*Department of Mathematics and Statistics, University of Massachusetts, Amherst, MA 01003-4515, USA*

<sup>2</sup>*Mathematics Department, University of Hartford,  
200 Bloomfield Ave., West Hartford, CT 06117, USA*

<sup>3</sup>*Institute of Photonics and Optical Science (IPOS),  
School of Physics, The University of Sydney, NSW 2006, Australia*

We consider the interaction of solitary waves in a model involving the well-known  $\phi^4$  Klein-Gordon theory, but now bearing both Laplacian and biharmonic terms with different prefactors. As a result of the competition of the respective linear operators, we obtain three distinct cases as we vary the model parameters. In the first the biharmonic effect dominates, yielding an oscillatory inter-wave interaction; in the third the harmonic effect prevails yielding exponential interactions, while we find an intriguing linearly modulated exponential effect in the critical second case, separating the above two regimes. For each case, we calculate the force between the kink and antikink when initially separated with sufficient distance. Being able to write the acceleration as a function of the separation distance, and its corresponding ordinary differential equation, we test the corresponding predictions, finding very good agreement, where appropriate, with the corresponding partial differential equation results. Where the two findings differ, we explain the source of disparities. Finally, we offer a first glimpse of the interplay of harmonic and biharmonic effects on the results of kink-antikink collisions and the corresponding single- and multi-bounce windows.

## I. INTRODUCTION

The study of nonlinear Klein-Gordon models is a topic that has a rich history. Many of the early developments on the subject have focused on the mathematically appealing theory of the inverse scattering transform and integrable systems [1–3], such as the famous sine-Gordon equation [4, 5]. However, more recently, the intriguing features stemming from non-integrable dynamics have been at the center of numerous studies centered around, e.g., the  $\phi^4$  model [6]. The latter has often been considered to be a prototypical system for phase transitions, ferroelectrics, and high-energy physics among other themes [4, 6]. Moreover, it has been a central point of both analytical and numerical explorations, involving kink interactions, collective coordinates, resonant dynamics (including with impurities) starting from the 1970’s and extending over nearly 5 decades [7–18] and even reaching to this day [19–21]; see also the recent recap of [22].

On the other hand, more recently, a diverse set of variants of the so-called nonlinear beam (or biharmonic) wave equation have been considered also; a collection of relevant examples includes, e.g., [23–26]. The corresponding models also span a diverse array of contexts, including, e.g., suspension bridges and the propagation of traveling waves therein. Another setting that has emerged very recently and has substantially promoted the relevance of biharmonic models has been the form of generalized nonlinear Schrödinger (NLS) type models in nonlinear optics in the context of the so-called “pure-quartic solitons” [27]. Not only has this type of dispersion engineering been realized in the lab, but it has also been used in the context of the so-called pure-quartic soliton laser [28]. Mathematical studies of the existence and stability of solitary waves of such equations are also ongoing [29–31].

It has, however, been recognized that the typical scenario involves (e.g., in the NLS experimental settings discussed above) both regular quadratic and quartic dispersion and that experimental settings have the ability to tune the interplay between the two [32]. This results in the form of a *generalized* NLS equation incorporating both quadratic and quartic dispersion and thus presenting the potential for engineering a situation involving competition between the two [32]. While the generalized NLS setting is the most canonical one to consider in the realm of nonlinear optics, in the present work we opt to consider the slightly simpler, yet highly informative, setting of a corresponding Klein-Gordon model. The rationale behind the latter choice involves the fact that the two models *share* the same existence properties, at least in one spatial dimension, yet the nature of the real field-theory renders the analytical calculations somewhat simpler, especially as regards the stability and dynamical implications of the inter-wave interactions.

Our aim in the present work is to formulate the existence problem of a single kink in a model incorporating quadratic and quartic dispersion in the presence of a  $\phi^4$  potential (this part will be entirely analogous to the corresponding generalized NLS case). Subsequently, we intend to explore the interaction of two such waves and identify their pairwise interaction force and how it depends on the model parameters. Subsequently, conclusions of the analytical theory will be tested against full numerical computations of the interaction dynamics. Lastly, collisions between two coherent structures will be simulated, and the possible scenarios thereof will be considered. Our aim is to reveal the possibility that either the biharmonic effect may dominate (yielding oscillatory tails and forces, equilibrium steady states of alternating stability etc.) or the harmonic effect will prevail (featuring exponential interactions and forces). The critical case between the two and its own intriguing behavior will be revealed as well. In our study of collisions and, in particular, in the case kinks and antikinks interact and eventually separate, we create velocity-out versus velocity-in curves. These curves show windows of velocity-in values for which we see different numbers of bounces before the coherent structures separate. We compare this behavior to both the “pure  $\phi^4$ ” case of Eq. 1 and the “pure biharmonic” special-case limits of the present model interpolating between them.

## II. MODEL SETUP & KINK-ANTI-KINK TAIL BEHAVIOR

The standard  $\phi^4$  Klein-Gordon theory yields the field equation

$$u_{tt} = u_{xx} - V'(u) \quad (1)$$

where  $V(u) = \frac{1}{2}(u^2 - 1)^2$ . In [30, 33], a variant of this equation was explored where the harmonic spatial derivative term was replaced by a biharmonic term of the form:

$$u_{tt} = -u_{xxxx} - V'(u). \quad (2)$$

Here, as indicated in the above section, motivated by the corresponding generalized NLS of [32], we explore a model incorporating the competition of the features of the two models:

$$u_{tt} = \alpha u_{xx} - \beta u_{xxxx} - V'(u) \quad (3)$$

where  $\alpha$  and  $\beta$  are assumed positive (to ensure the competition referred to above) and the potential function  $V(u)$  is taken as before. When we pick  $\alpha = 1$  and  $\beta = 0$ , we get Eq. (1) and when we pick  $\alpha = 0$  and  $\beta = 1$ , we get Eq. (2). Notice that while one of the coefficients could be scaled out via a rescaling of space, we maintain both coefficients, in order to maintain the tractability of the special case limits of (0,1) and (1,0), i.e., biharmonic and harmonic respectively.

A central consideration of the present work is to explore both the features of a single solitary wave, but also to examine the interaction between two such waves, a kink and an antikink. We will use a method developed by Manton (as in [33, 34]) to find the force between a separated kink and antikink as a function of the separation distance. To do this we must first determine the tail behavior for a single kink or antikink. Once the force is determined, we can use the corresponding acceleration to generate an ordinary differential equation (ODE), whose behavior can then be compared to the soliton trajectories of Eq. (3), i.e., the corresponding partial differential equation (PDE). As long as the separation distance between kink and antikink remains sufficiently large, the agreement between ODE and PDE should be quite good. However, in cases where the kink and antikink approach each other at distances comparable to their respective widths, then it is no longer obvious that the ODE model should be an adequate description of the full PDE dynamics and the exchanges of energy between the different modes present in the latter [6]. We will explore both the former agreement (at large distances) and the latter deviations (at short ones) in the numerical results below. In order to determine the tail behavior of a single kink we proceed as follows. Substituting  $\phi(x) = u(t, x)$  into Eq. (3) we get the steady-state equation

$$\alpha\phi'' - \beta\phi^{(iv)} - V'(\phi) = 0 \quad (4)$$

To examine the relevant asymptotics, we substitute  $\phi = 1 - \varepsilon e^{\lambda x}$  into the Eq. (4). Neglecting terms of  $\varepsilon^2$  and higher (i.e., linearizing), for the above mentioned  $\phi^4$  potential, we get

$$-\alpha\lambda^2 + \beta\lambda^4 + 4 = 0 \quad (5)$$

It is easy to show that the roots of this equation are real for  $\alpha \geq 4\sqrt{\beta}$  and complex for  $\alpha < 4\sqrt{\beta}$ . In particular, for  $\alpha < 4\sqrt{\beta}$ :

$$\begin{aligned} \lambda_1 &= \frac{1}{2}\sqrt{\frac{4\sqrt{\beta} + \alpha}{\beta}} + i\frac{1}{2}\sqrt{\frac{4\sqrt{\beta} - \alpha}{\beta}}, & \lambda_2 &= \frac{1}{2}\sqrt{\frac{4\sqrt{\beta} + \alpha}{\beta}} - i\frac{1}{2}\sqrt{\frac{4\sqrt{\beta} - \alpha}{\beta}} \\ \lambda_3 &= -\frac{1}{2}\sqrt{\frac{4\sqrt{\beta} + \alpha}{\beta}} + i\frac{1}{2}\sqrt{\frac{4\sqrt{\beta} - \alpha}{\beta}}, & \lambda_4 &= -\frac{1}{2}\sqrt{\frac{4\sqrt{\beta} + \alpha}{\beta}} - i\frac{1}{2}\sqrt{\frac{4\sqrt{\beta} - \alpha}{\beta}} \end{aligned}$$

for  $\alpha = 4\sqrt{\beta}$  (critical case), the degenerate roots are:

$$\lambda_{1,2} = \sqrt{\frac{\alpha}{2\beta}}, \quad \lambda_{3,4} = -\sqrt{\frac{\alpha}{2\beta}}$$

and for  $\alpha > 4\sqrt{\beta}$ :

$$\begin{aligned} \lambda_1 &= \sqrt{\frac{\alpha - \sqrt{\alpha^2 - 16\beta}}{2\beta}}, & \lambda_2 &= \sqrt{\frac{\alpha + \sqrt{\alpha^2 - 16\beta}}{2\beta}} \\ \lambda_3 &= -\sqrt{\frac{\alpha - \sqrt{\alpha^2 - 16\beta}}{2\beta}}, & \lambda_4 &= -\sqrt{\frac{\alpha + \sqrt{\alpha^2 - 16\beta}}{2\beta}} \end{aligned}$$

For real  $\lambda$ , similarly to the pure  $\phi^4$  case, our model for the tail behavior is

$$be^{-ax} + de^{-cx}, \quad (6)$$

for the critical case with the double roots the model is

$$be^{-ax}(x - d) \quad (7)$$

(accounting for the relevant generalized eigenvector) and for the complex  $\lambda$  case (similarly to the pure biharmonic one), the model is

$$be^{-ax} \cos(c(x-d)). \quad (8)$$

We also know that in the real case  $a = \lambda_1 = \sqrt{\frac{\alpha - \sqrt{\alpha^2 - 16\beta}}{2\beta}}$  and  $c = \lambda_2 = \sqrt{\frac{\alpha + \sqrt{\alpha^2 - 16\beta}}{2\beta}}$  and in the complex case  $a = \text{Re}(\lambda) = \frac{1}{2}\sqrt{\frac{4\sqrt{\beta} + \alpha}{\beta}}$  and  $c = \text{Im}(\lambda) = \frac{1}{2}\sqrt{\frac{4\sqrt{\beta} - \alpha}{\beta}}$ , while in the critical case  $a = \sqrt{\frac{\alpha}{2\beta}}$ . We use curve fitting to get the other parameters  $b$  and  $d$ . The results are in Table I for a sequence of prototypical case examples that we have considered.

$\alpha$	$\beta$	$\lambda$	Tail behavior
0	1	1-1i	$0.9700e^{-x} \cos(x - 0.4083)$
1	1	1.1180-0.8660i	$1.205e^{-1.118x} \cos(0.8660(x - 0.9909))$
2	1	1.2247-0.7071i	$1.793e^{-1.225x} \cos(0.7071(x - 1.824))$
3	1	1.3229-0.5000i	$3.614e^{-1.323x} \cos(0.5(x - 3.299))$
3.5	1	1.3693-0.3536i	$6.662e^{-1.369x} \cos(0.3536(x - 4.942))$
4	1	1.4142	$3.363e^{-1.414x} (x - 0.9786)$
4.5	1	1.1042, 1.8113	$4.451e^{-1.104x} - 12.92e^{-1.811x}$
5	1	1, 2	$3.354e^{-x} - 25.64e^{-2x}$
6	1	0.8740, 2.2882	$2.679e^{-0.8740x} - 157.4e^{-2.288x}$
1	0	2	$2e^{-2x}$

TABLE I. Single Kink Tail Behavior for different model parameter  $(\alpha, \beta)$  in columns 1 and 2. Column 3 yields the corresponding (spatial) eigenvalues and column 4 the functional form providing the optimal fit to the tail behavior. One can read off the values of  $a, b, c, d$  in column 4 by referring to Equations (6), (7), (8).

In Figure 1 we show a single kink,  $\phi_K(x)$ , in the top three panels and the tail-behavior of each kink in the bottom three panels for the cases  $\alpha = 1$ ,  $\alpha = 4$ ,  $\alpha = 5$  with  $\beta = 1$  (respectively, left to right). For the tail behavior we graph the right tail of  $1 - \phi_K(x)$  multiplied by  $\exp(kx)$  as well as a model fitted to the tail of  $1 - \phi_K(x)$ , also multiplied by  $\exp(kx)$  (appropriate for  $x$  sufficiently large). The value of  $k$  is equal to the real part  $\text{Re}(\lambda)$  in the complex case,  $\lambda$  in the critical case, and the smaller (in absolute value)  $\lambda$  in the real case (corresponding to the slow decay). We can observe an excellent agreement in the oscillatory case (especially factoring in that we have multiplied the expression by an exponential, hence any deviation in the exponent would lead to an exponential growth). Similarly, also a remarkable fit can be discerned even in the critical case, revealing the underlying linear dependence modulating the exponential decay of the generalized eigenvector in this setting. The exponential case (originally doubly exponential turned into a single exponential upon multiplication by  $\exp(kx)$ ) is found to be less accurate. In the latter case of two real  $\lambda$  an improved fit can be obtained to the model  $be^{-ax} + de^{-cx}$  if  $c$  is left as a free parameter in the curve-fitting process (rather than using the value specified above which results from Eq. (5)). It is an interesting question for future work, whether a weakly nonlinear theory can capture more accurately the correction to the leading exponential dependence; however, for our present purposes, the current prediction capturing adequately the leading order exponential tail behavior will suffice.

### III. THE FORCE BETWEEN KINK AND ANTIKINK

In order to find the force or acceleration between kink and antikink, we use the approach of Manton as in [33, 34]; see also [33] for details of the calculation in the case where  $\alpha = 0$  and  $\beta = 1$ . We now briefly review some of the details of this force calculation. Consider the momentum  $P = -\int_{x_1}^{x_2} u_t u_x dx$  on the interval  $[x_1, x_2]$  ( $P$  is conserved when the integral is over the entire real line). Differentiating under the integral and using Eq. (3) we find that the force is given by

$$\frac{dP}{dt} = F = \left[ -\frac{1}{2}u_t^2 - \alpha\frac{1}{2}u_x^2 + \beta u_x u_{xxx} - \beta\frac{1}{2}u_{xx}^2 + V(u) \right]_{x_1}^{x_2}. \quad (9)$$

For a field configuration that is static or almost so, we can ignore the first term in the right hand side bracket of Eq. (9). We consider a configuration

$$u(t, x) = \phi(x) = \phi_K(x + X(t)) + \phi_{AK}(x - X(t)) - 1, \quad (10)$$

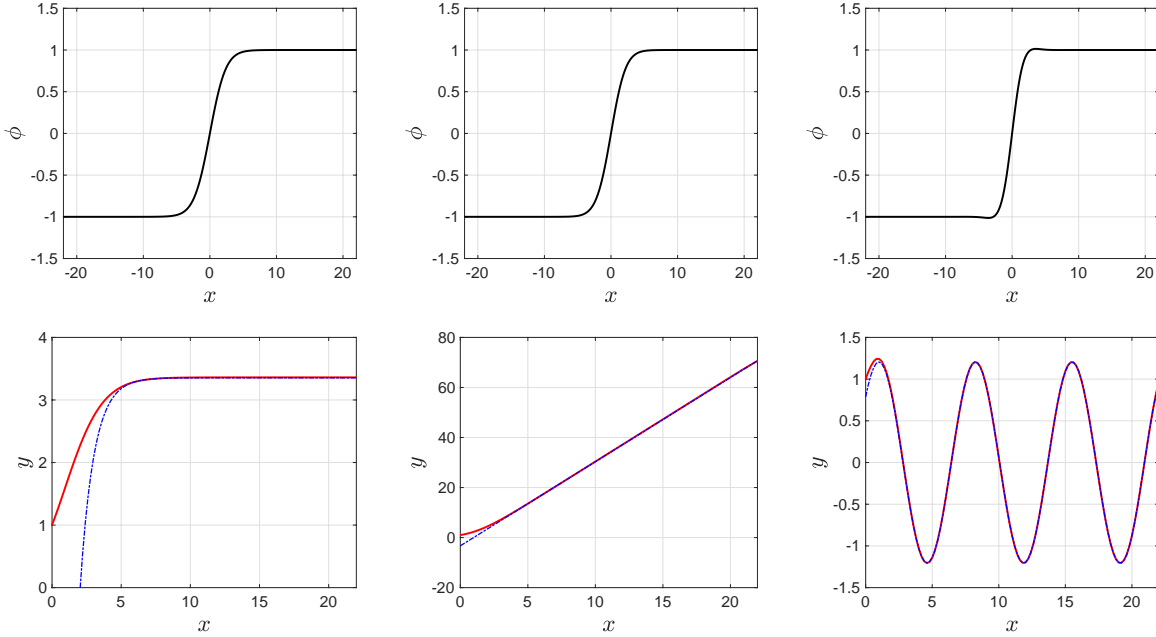


FIG. 1. The top three panels show a single kink,  $\phi_K(x)$ , for each of the cases  $\alpha = 1$ ,  $\alpha = 4$ ,  $\alpha = 5$  and  $\beta = 1$  (respectively, left to right). The bottom three panels illustrate the behavior of the right-side tails of these kinks by graphing  $1 - \phi_K(x)$  multiplied by  $\exp(kx)$ , where  $k$  (positive) is  $\text{Re}(\lambda)$  in the complex case,  $\lambda$  in the critical case, and the smaller (in absolute value)  $\lambda$  in the real case. Superimposed are the fitted curves, also multiplied by  $\exp(kx)$ . In all cases the red solid curve is  $\exp(kx)(1 - \phi_K)$ . The blue dash-dot curve is the fitted equation multiplied by  $\exp(kx)$ ; the specific equations for each case are  $y = 1.205 \cos(0.8660(x - 0.9890))$ ,  $y = 3.274(x - 0.8606)$  and  $y = 3.308 - 14.9e^{-x}$  (right to left respectively)

where  $-X(t)$  is the position of the kink and  $X(t)$  is the position of the antikink, which represents a kink-antikink pair approaching each other (as  $t$  gets larger). Then, set  $\eta = 1 - \phi$ ,  $\eta_K = 1 - \phi_K$  and  $\eta_{AK} = 1 - \phi_{AK}$  (where  $\phi_{AK}$  is an antikink solution to Eq. (4)). Evaluating Eq. (9) from  $x_1 = x$  to  $x_2 \rightarrow \infty$  results in

$$F = \alpha(\eta_K)_x(\eta_{AK})_x - \beta(\eta_K)_x(\eta_{AK})_{xxx} - \beta(\eta_K)_{xxx}(\eta_{AK})_x + \beta(\eta_K)_{xx}(\eta_{AK})_{xx} - 4(\eta_K)(\eta_{AK}), \quad (11)$$

where we assume that the kink-antikink separation  $2X$  is large. We have also assumed that  $|x| \ll X$  and have used the approximation  $V(\phi) = V(1 - \eta) \approx 2\eta^2$ . Note that only the cross terms are left at this point.

For the **complex case** the model for the tail behavior is  $\eta_K = be^{-ax} \cos(c(x - d))$ , appropriate for  $x$  sufficiently large.

Carrying out the derivatives in Eq. (11) and using  $a = \text{Re}(\lambda) = \frac{1}{2}\sqrt{\frac{4\sqrt{\beta} + \alpha}{\beta}}$  and  $c = \text{Im}(\lambda) = \frac{1}{2}\sqrt{\frac{4\sqrt{\beta} - \alpha}{\beta}}$  we get the following expression for the force:

$$F = -2\sqrt{\frac{16\beta - \alpha^2}{\beta}} b^2 e^{-X\sqrt{\frac{4\sqrt{\beta} + \alpha}{\beta}}} \cos\left(\sqrt{\frac{4\sqrt{\beta} - \alpha}{\beta}}(X - d) + \theta\right). \quad (12)$$

Here, we have that  $\theta \in [0, \frac{\pi}{2}]$  such that  $\tan \theta = \frac{\alpha}{\sqrt{16\beta - \alpha^2}}$ .

For the **critical case** the model for the tail behavior is  $be^{-ax}(x - d)$ . This, upon substituting  $a = \sqrt{\frac{\alpha}{2\beta}}$  and  $\alpha = 4\sqrt{\beta}$  results in the force formula:

$$F = -8b^2\sqrt{2\alpha}e^{-2aX}\left(X - \frac{\sqrt{2\alpha}}{4} - d\right), \quad (13)$$

once again featuring a functional form reminiscent of that of the kink tail.

For the **real case** the tail behavior is  $be^{-ax} + de^{-cx}$  and the force becomes

$$F = -b^2e^{-2Xa}(a^2\alpha - 3a^4\beta + 4) - d^2e^{-2Xc}(c^2\alpha - 3c^4\beta + 4),$$

$\alpha$	$\beta$	Mass	Acceleration
0	1	1.1852	$6.351e^{-2x} \cos(2x - 0.8166)$
1	1	0.9540	$11.79e^{-2.236x} \cos(1.732x - 1.464)$
2	1	0.8052	$27.66e^{-2.4494x} \cos(1.4142x - 2.0559)$
3	1	0.7031	$98.30e^{-2.6458x} \cos(x - 2.451)$
3.5	1	0.6633	$259.1e^{-2.7386x} \cos(0.7072x - 2.429)$
4	1	0.6290	$407.0e^{-2.828x} (x - 1.686)$
4.5	1	0.5991	$166.2e^{-2.208x} - 3769e^{-3.623x}$
5	1	0.5728	$117.8e^{-2x} - 27545e^{-4x}$
6	1	0.5287	$92.75e^{-1.748x} - 2194577e^{-4.576x}$
1	0	4/3	$24e^{-4x}$

TABLE II. Mass and acceleration as a function of the half-separation distance  $x$  of the kink and antikink.

where:

$$a = \sqrt{\frac{\alpha - \sqrt{\alpha^2 - 16\beta}}{2\beta}} \quad \text{and} \quad c = \sqrt{\frac{\alpha + \sqrt{\alpha^2 - 16\beta}}{2\beta}}. \quad (14)$$

Using these values the force formula can be written as

$$F = \frac{\alpha^2 - 16\beta - \alpha\sqrt{\alpha^2 - 16\beta}}{\beta} b^2 e^{-2Xa} + \frac{\alpha^2 - 16\beta + \alpha\sqrt{\alpha^2 - 16\beta}}{\beta} d^2 e^{-2Xc}. \quad (15)$$

Notice that the coefficient of the slow term is always negative while the coefficient of the fast term is always positive. Dividing the above formulae for the force by the mass gives the results in the acceleration column of Table II. The values for  $b$  and  $d$  are determined by curve fitting the tail of a single kink, and are shown in Table I.

Next, we integrate the expressions for the force on a kink to get the potential energy for each case, and also find all fixed points and their stability type. For the potential function in the complex case we have

$$U = -b^2 \sqrt{\frac{16\beta - \alpha^2}{2\sqrt{\beta}}} e^{-X\sqrt{\frac{4\sqrt{\beta} + \alpha}{\beta}}} \cos\left(\sqrt{\frac{4\sqrt{\beta} - \alpha}{\beta}} (X - d) + \vartheta\right) \quad (16)$$

for  $\vartheta \in [0, \frac{\pi}{2}]$  such that  $\tan \vartheta = \frac{\sqrt{4\sqrt{\beta} + \alpha}}{\sqrt{4\sqrt{\beta} - \alpha}}$ . For saddle points we have

$$X^*(k) = d + \left(\frac{\pi}{2} + 2k\pi - \theta\right) \sqrt{\frac{\beta}{4\sqrt{\beta} - \alpha}},$$

and for centers we get

$$X^*(k) = d + \left(\frac{\pi}{2} + (2k + 1)\pi - \theta\right) \sqrt{\frac{\beta}{4\sqrt{\beta} - \alpha}}.$$

For the critical case (repeated  $\lambda$ ) the potential function is

$$U = -2b^2 \alpha e^{\frac{-4\sqrt{2}}{\sqrt{\alpha}} X} \left(X - d - \frac{\sqrt{2\alpha}}{8}\right) \quad (17)$$

and the center is given by

$$X^* = d + \frac{\sqrt{2\alpha}}{4}.$$

For the real case we have the potential function

$$U = -b^2 a \sqrt{\alpha^2 - 16\beta} e^{-2aX} + d^2 c \sqrt{\alpha^2 - 16\beta} e^{-2cX}, \quad (18)$$

and the center:

$$\frac{1}{2(c - a)} \left(\log \frac{c^2 d^2}{a^2 b^2}\right),$$

with  $a$  and  $c$  as given in Eq. (14).

#### IV. COMPARISON OF ODE AND PDE MODELS

Using the expressions for the force we can now write an ODE for the time evolution of the kink and antikink position for any given  $(\alpha, \beta)$  combination. In Table II we have divided the force by the numerically calculated mass and used the curve-fitted values for  $b$  and  $d$  to get an acceleration expression for specific values of  $\alpha$  and  $\beta$ . The corresponding ODE is then  $\ddot{X} = -dU/dX$ , where the acceleration of the right hand side is provided in Table II. This ODE for the position of the one coherent structure (while the other one is symmetrically located) is amenable to a phase portrait analysis, as shown in Figure 2 and a comparison with the corresponding PDE results of Eq. (3) can be obtained both at that level and at the spatio-temporal evolution one as shown in Fig. 3.

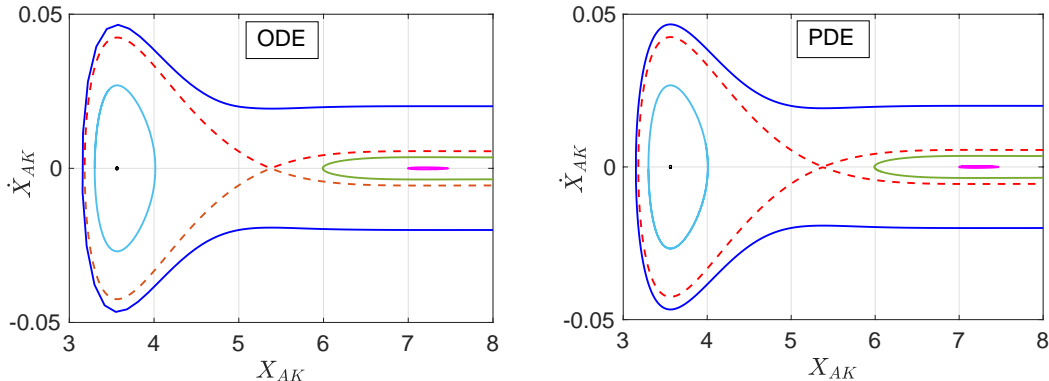


FIG. 2.  $\alpha = 1, \beta = 1$ , Phase portrait of the ODE Equation (ODE) in comparison with Eq. (3) (PDE). The blue solid curve corresponds to  $X_{AK}(0) = 8, \dot{X}_{AK}(0) = -0.02$ . The red dash-dotted curve:  $X_{AK}(0) = 8, \dot{X}_{AK}(0) = -0.00555$ . The light blue closed orbit:  $X_{AK}(0) = 3.3, \dot{X}_{AK}(0) = 0$ . The green curve corresponds to  $X_{AK}(0) = 8, \dot{X}_{AK}(0) = -0.00356$ . The pink solid closed orbit:  $X_{AK}(0) = 7.4, \dot{X}_{AK}(0) = -0.0002$ .

In Figure 2 we show trajectories for the case  $\alpha = 1$  and  $\beta = 1$  (complex case) that illustrate behavior near the steady states of the PDE (the fixed points of the ODE). For these cases, there is clearly excellent agreement, between the ODE and PDE phase planes which validates our force calculations. The calculated force laws work well as long as the separation between kink and antikink is sufficiently large. In the case of the PDE, we identify the motion of the coherent structure by using the intersection of the kink or antikink with the horizontal axis as the position, and also find the corresponding speed, and thus extract an effective phase portrait to be compared with the ODE results. In Figure 3 we show two of the trajectories from Figure 2 as contour plots of the PDE with the ODE trajectory superimposed on top (in blue). The left one among them is a robust oscillation around a stable fixed point in the form of a center (the light blue curve in Figure 3). The other is a trajectory that is scattered from the innermost potential energy barrier –due to the presence of the innermost saddle point, corresponding to a maximum– of the effective energy landscape and is thus reflected. In this case, we see that the kinks do not make it to a collision but are rather reflected due to their interaction landscape before the collision.

For another perspective on the quantification of the agreement between PDE and ODE results, see Figure 4. In the left panel of this figure, we show the potential energy plot of the ODE, again for  $\alpha = 1, \beta = 1$ , in blue (using Eq. 16). The data points represent the potential energies of the steady states of the PDE calculated using the PDE energy  $E = \int \frac{1}{2}\alpha u_x^2 + \frac{1}{2}\beta u_{xx}^2 + \frac{1}{2}(u^2 - 1)^2 dx$  of the associated steady state configurations. The corresponding steady-states themselves are shown in the same figure, right panel. Note that since the calculated potential energy curve of the ODE approaches zero as the separation distance increases, the potential energies of the steady states of the PDE must also be normalized (i.e., calibrated) so that the limiting value is zero (by subtracting the potential energy of a steady state with very large separation). Again, clearly, the local maximum and minimum values of the ODE energy landscape coincide with the potential energies of the corresponding steady states of the PDE. The local minima correspond to stable steady states of the PDE (centers of the ODE) and the local maxima correspond to unstable steady states of the PDE (saddle points of the ODE). Importantly, aside from the center-most potential energy maximum where the kink structures are so close that we cannot identify them as independent entities (and thus we do not expect the collective coordinate characterization to be as accurate), we observe that the agreement is very good. We remind the reader that the presence of this oscillatory energy landscape, its associated minima (centers) and maxima (saddles), and the respective stationary PDE configurations are distinctive features of the prevalence of the biharmonic term and are genuinely absent in the harmonic case (and more generally for  $\alpha > 4\sqrt{\beta}$ , when the harmonic contribution is dominant).

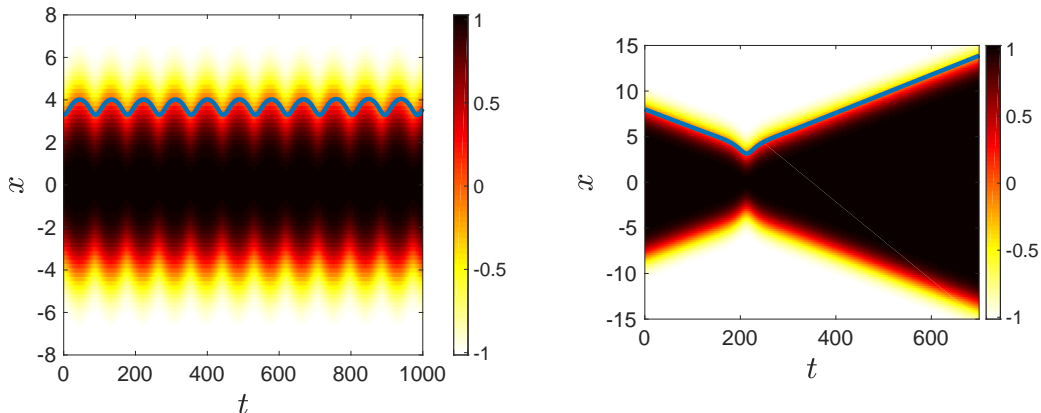


FIG. 3.  $\alpha = 1, \beta = 1$ . Comparisons of the PDE contour plot of the displacement field  $u(x;t)$  and the ODE trajectory. (blue solid curve). Left:  $x_0 = 3.3, v_{in} = 0$ . This corresponds to the closed orbit (light blue) in Fig. 2. Right:  $x_0 = 8, v_{in} = -0.02$ . This corresponds to blue solid curve in Fig. 2.

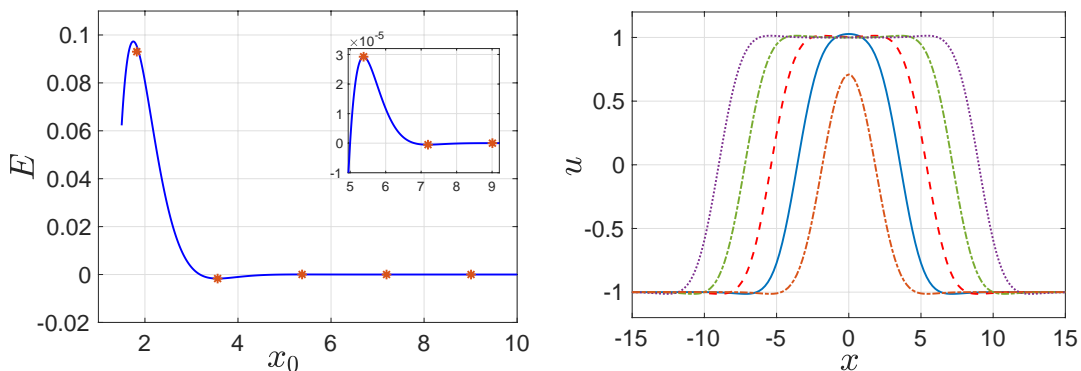


FIG. 4. The left panel shows the energy vs  $x_0$  for  $\alpha = 1, \beta = 1$ . Blue curve is twice the potential function of the ODE for the complex case (given in Eq. (16)). The data points are the (normalized) potential energies of the steady states of the PDE at  $x_0 = 1.825, 3.56, 5.38, 7.19, 9.01$  which are shown in the right panel. The need to multiply the potential function of the ODE by two when comparing ODE and PDE stems from the fact that the energy calculation using a steady state of the PDE involves two solitons - kink and antikink. The right panel presents the static, equilibrium solutions corresponding to  $x_0 \approx 1.825$  (orange dashed-dot curve),  $x_0 \approx 3.56$  (blue solid curve),  $x_0 \approx 5.38$  (red dashed curve),  $x_0 \approx 7.19$  (green dashed-dot curve) and  $x_0 \approx 9.01$  (purple dotted curve). Note that the steady state for the PDE occurs at  $x_0 \approx 1.825$  but the fixed point of the ODE is at  $x_0 \approx 1.75$ .

While in Figure 2 we showed example phase portraits that resulted in very proximal correspondence between PDE and ODE (for the complex case), in Figure 5 we show phase trajectories for both the real and complex cases that illustrate at what point the PDE and ODE solution curves may depart from each other (recall that the dash-dotted green line represents the position of the antikink as measured by its intersection with the horizontal axis). In these cases, the kink and antikink get too close for the force law to remain valid. One can see that in the real case of the left panel this occurs at about  $X_{AK} = 3$ , while in the complex case of the right panel at about  $X_{AK} = 2$ . Note also that the green curve (position of the antikink) indicates the formation of a bound state which is losing energy (in a way



somewhat akin to a stable spiral but keeping in mind that in a bound state there are no longer an identifiable kink and antikink). Here, the important differences of the PDE dynamics from the conservative ODE of 1 degree-of-freedom (dof) become evident. The latter being energy conserving can only reflect in some way, while the former can transfer energy from the kink translational motion to other degrees of freedom (internal ones or radiation ones [6]), thus leading to the effective translational energy dispersion and thus the apparent trapping of the kinks into a so-called bion state. Successive “breathings” of this bion state at the PDE level are mirrored in the progressively inward green curves (carrying less and less energy). At the ODE level, we make two more minor (in terms of the bigger picture of our story), yet technically relevant observations. Given the absence of ODE-PDE correspondence in the right panel we stop the ODE evolution once the kink-antikink pair directly collides (i.e., at  $X = 0$ ). On the other hand, the left panel has another intriguing but non-physical trait: the double exponential force (of opposite signs between the two exponentials) results in a landscape with a local minimum very close to  $X = 0$ . While this would result in a turning point of  $X \neq 0$ , we have found this feature to be an artifact of the theory and its lack of accuracy in the immediate vicinity of  $X = 0$ . Let us reiterate, also in light of the above remarks, that the ODE models are based only on the behavior of the tails of the kinks and antikinks. When a kink and antikink are involved in an interaction, the model makes sense only when the structures are well-separated. Therefore the ODE model should not be expected to reflect the actual behavior of the system beyond the point where the waves are at a distance comparable to or smaller than their width, at which time they essentially forego their individual character.

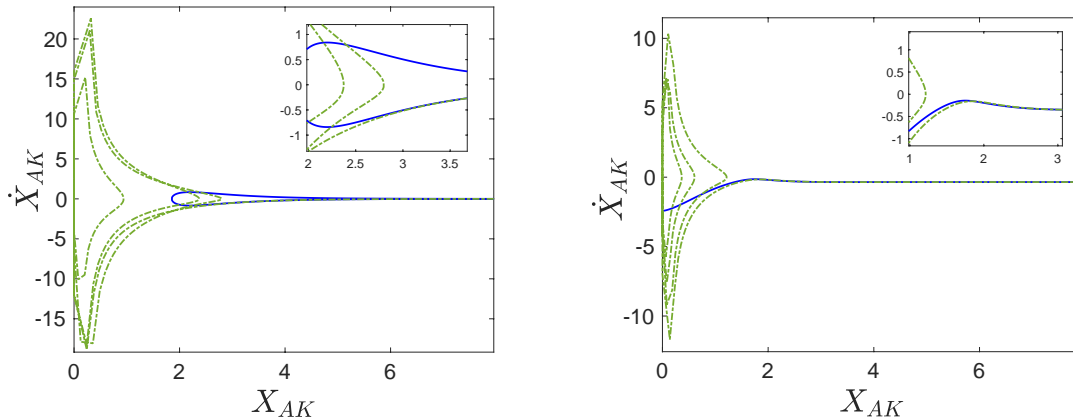


FIG. 5. The left panel shows phase plots for the real  $\lambda$  case of  $\alpha = 5$  and  $\beta = 1$  using initial conditions  $X_{AK}(0) = 8$  and  $\dot{X}_{AK}(0) = -0.003593$ . The right panel illustrates phase plots for the complex  $\lambda$  case of  $\alpha = 1$  and  $\beta = 1$  using initial conditions  $X_{AK}(0) = 8$  and  $\dot{X}_{AK}(0) = -0.35$ . In both cases, the ODE is shown by the blue solid curve and the PDE by the green dash-dotted curve. Insets show at what points the ODE model diverges from the PDE model. The ODE trajectory in the right panel is stopped at the point when  $X_{AK} = 0$  because it becomes physically unrealistic beyond that point.

In Figure 6 we show contour plots for the same values of  $\alpha$  and  $\beta$  and the same initial conditions as in Figure 5, again with the ODE solution curves superimposed. I.e., these panels represent the spatio-temporal contour representation of the failure of the ODE theory to capture the PDE dynamics, as explained in the above discussion. As in Figure 5 we can see that the ODE tracks the PDE simulation until around the time that the collision occurs. As a result of the latter, at the PDE level, a bound state emerges, while in the case of the ODE, the conservative nature of the 1 dof system does not allow any scenario other than reflection.

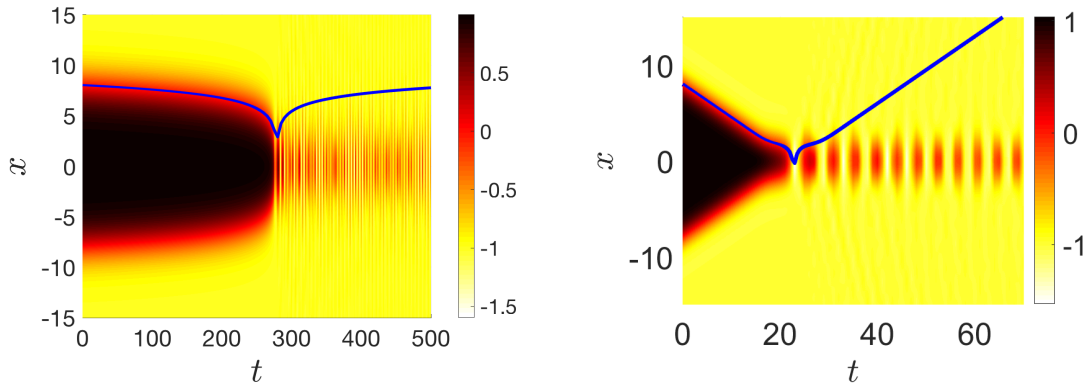


FIG. 6. Contour plots of the PDE corresponding to the same parameter values and initial conditions as in the corresponding panels of Figure 5. The ODE trajectory is superimposed in blue.

## V. VELOCITY IN VERSUS VELOCITY OUT CURVES AND SOLITON COLLISIONS

We now investigate kink-antikink collisions in the context of escape velocity ( $v_{out}$ ) and multi-bounce windows as a function of incoming velocity ( $v_{in}$ ), in line with the extensive literature on the subject discussed in the Introduction (for a relatively recent summary in the  $\phi^4$  case, see, e.g., [6]). For the latter model, it has been shown that there exists a critical  $v_{in}$  value, which we label  $v_{crit}$ , such that for  $v_{in} > v_{crit}$ , the kink and antikink interact once and then separate forever. For  $v_{in} < v_{crit}$  the kink and antikink can form a bound state, or can interact (bounce) any number of times, depending on  $v_{in}$ , before separating forever. Furthermore, it is well-established since the work of [14] for the  $\phi^4$  model, that the bounce windows corresponding to different numbers of bounces are nested in a fractal pattern. For example, three bounce windows occur at the edges of two-bounce windows, four bounce windows occur at the edges of three-bounce windows, and so on. Also, the  $v_{in} - v_{out}$  graph for a given window has the appearance of an inverted parabola, with the  $v_{out}$  values going to zero at the edges of the window.

For a model with only a biharmonic term ( $\alpha = 0$  in this paper) it was shown in [30] that two critical  $v_{in}$  values exist, with  $v_{1,crit} < v_{2,crit}$ .  $v_{2,crit}$  is similar to  $v_{crit}$  for the  $\phi^4$  model in that for  $v_{in} > v_{2,crit}$  the kink and antikink interact once and then separate. For  $v_{in} < v_{1,crit}$  the kink and antikink repel elastically before interacting. For  $v_{1,crit} < v_{in} < v_{2,crit}$  the kink and antikink form a bound state. Near both critical values, we see oscillations in the  $v_{in} - v_{out}$  graph, where the frequency of the oscillations rapidly increases as the critical values are approached.

In the model described in this paper, which is a mixture of the two cases just described, we find that by fixing  $\beta$  at  $\beta = 1$  and letting  $\alpha$  increase from zero to six, we see a transition from one case to the other. As  $\alpha$  is increased, more and more bounce windows begin to populate the region between  $v_{1,crit}$  and  $v_{2,crit}$ . At first these new bounce windows display oscillations in the  $v_{in} - v_{out}$  graphs near the edges of the windows, similar to what is seen in the bound-state region of the pure biharmonic case. With increasing  $\alpha$  the oscillations diminish and the  $v_{out}$  values at the edges of each window begin to approach zero as in the pure  $\phi^4$  case. We will showcase these features qualitatively in the results that follow. Nevertheless, the delicate nature of the associated computations renders especially difficult the identification of effective “critical points” where the behavior changes from the one reminiscent of the pure biharmonic problem to that reminiscent of the pure harmonic one. In the case of the critical velocities, by rescaling we are able to relate the solutions to Eq. (3) for general  $\alpha$  and  $\beta = 1$  to other combinations of  $\alpha$  and  $\beta$ , as is now shown.

Let  $u^{1,\beta}$  be a solution to

$$u_{tt} = u_{xx} - \beta u_{xxxx} + 2u - 2u^3.$$

and consider the coordinate transformation

$$x \mapsto \xi = \frac{x}{a}.$$

In the new coordinate system the solution can be rewritten as  $u^{1,\beta}(x, t) = \tilde{u}(\xi, t)$ . Of course,  $u_{tt}^{1,\beta} = \tilde{u}_{tt}$  and  $u_x^{1,\beta} = \frac{1}{a}\tilde{u}_\xi$ , therefore  $\tilde{u}$  obeys the equation

$$\tilde{u}_{tt} = \frac{1}{a^2}\tilde{u}_{\xi\xi} - \frac{\beta}{a^4}\tilde{u}_{\xi\xi\xi\xi} + 2\tilde{u} - 2\tilde{u}^3.$$

For  $a^4 = \beta$  we get

$$\tilde{u}_{tt} = \frac{1}{\sqrt{\beta}} \tilde{u}_{\xi\xi} - \tilde{u}_{\xi\xi\xi\xi} + 2\tilde{u} - 2\tilde{u}^3$$

so,  $\tilde{u}(\xi, t) \equiv u^{\alpha,1}(\xi, t)$  or,

$$u^{1,\beta}(x, t) = u^{\alpha,1}\left(\frac{x}{\beta^{1/4}}\right)$$

for  $\alpha = \frac{1}{\sqrt{\beta}}$ .

Therefore we can obtain solutions to the model for the parameters  $\alpha = 1$  and  $\beta$ , using the solution for parameters  $\alpha$  and  $\beta = 1$ . Then, using this coordinate transformation, we find that the critical velocity  $v_{1,crit}^{1,\beta}$  of the solution  $u^{1,\beta}$  can be expressed in terms of the corresponding critical velocity  $v_{1,crit}^{\alpha,1}$  of the  $u^{\alpha,1}$  solution as

$$v_{1,crit}^{1,\beta} = \frac{dx}{dt} = a \frac{d\xi}{dt} = \beta^{1/4} v_{1,crit}^{\alpha,1}, \quad (19)$$

where  $\alpha = \frac{1}{\sqrt{\beta}}$ .

Notice that when  $\beta$  becomes large enough, we get  $v_{1,crit}^{\alpha,1} \approx v_{1,crit}^{0,1}$ , so

$$v_{1,crit}^{1,\beta} \sim \beta^{1/4} v_{1,crit}^{0,1}.$$

Similarly

$$v_{1,crit}^{\alpha,1} \sim \sqrt{\alpha} v_{1,crit}^{1,0}.$$

Furthermore, the above equations hold when  $v_{1,crit}^{\alpha,1}$  is replaced by  $v_{2,crit}^{\alpha,1}$ .

In Figure 7 we show graphs of  $v_{1,crit}$  versus  $\alpha$  for  $\beta = 1$  (left panel) and  $v_{1,crit}$  versus  $\beta$  for  $\alpha = 1$  (right panel). Figure 8 is similar, but for  $v_{2,crit}$ . The blue circles on all panels are obtained by the numerical simulation of Eq. (3) where the left panels represent  $v_{1,crit}$  vs  $\alpha$  when  $\beta = 1$  and the right panels represent  $v_{1,crit}$  vs  $\beta$  when  $\alpha = 1$ . In the panels of both figures, the red curves are obtained from the transformation given by Eq. (19) (plotted without markers for the transformed points and with connecting lines in order to make the graph more readable). The red curves are included to demonstrate the validity of Eq. (19) in comparison with direct PDE simulations.

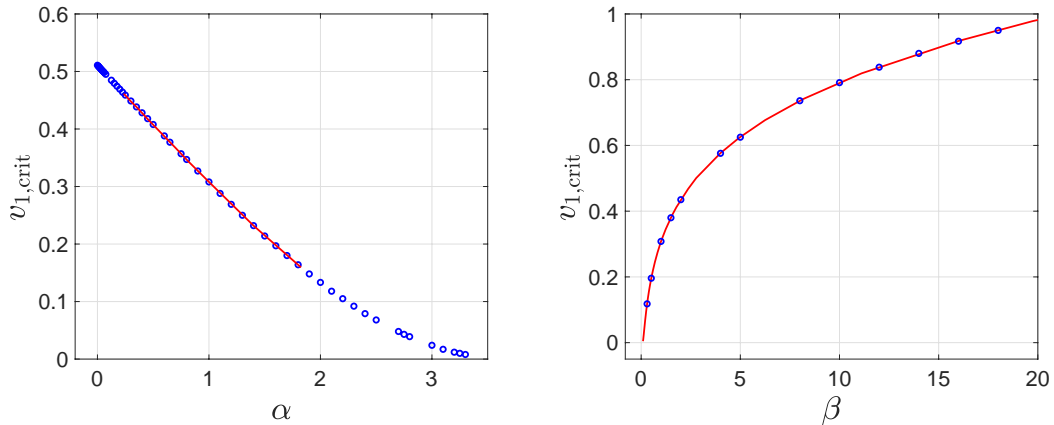


FIG. 7. The blue circles on both panels are obtained by the numerical simulation of Eq. (3) where left panel represents  $v_{1,crit}$  vs  $\alpha$  when  $\beta = 1$  and the right panel represents  $v_{1,crit}$  vs  $\beta$  when  $\alpha = 1$ . The red solid curve on the left panel is obtained by applying the formula  $v_{1,crit}^{\alpha,1} = \sqrt{\alpha} v_{1,crit}^{1,\beta}$  where  $\beta = \frac{1}{\alpha^2}$  to the numerically obtained data (blue circles) on the right. The red solid curve on the right panel is obtained by applying the formula  $v_{1,crit}^{1,\beta} = \beta^{1/4} v_{1,crit}^{\alpha,1}$  to the numerically obtained data (blue circles) on the left.

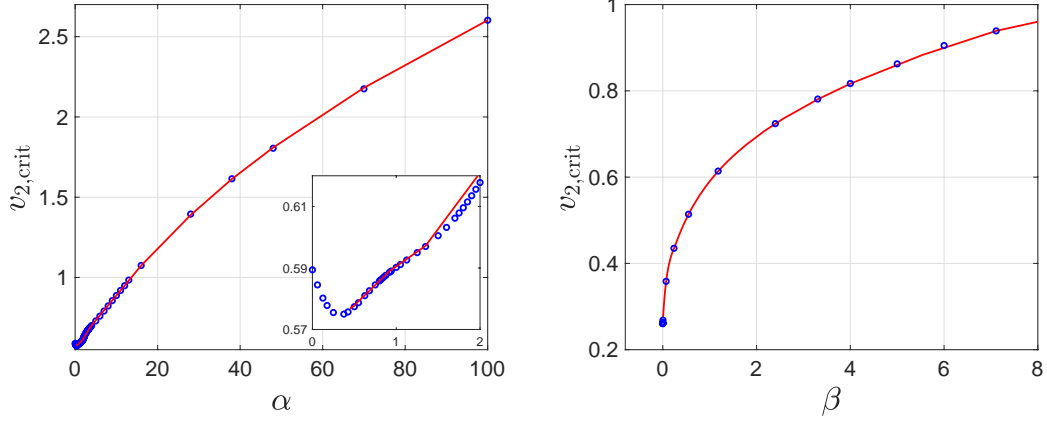


FIG. 8. The left panel shows  $v_{2,crit}$  vs  $\alpha$  when  $\beta = 1$  and the right panel shows  $v_{2,crit}$  vs  $\beta$  when  $\alpha = 1$ . The blue circles and the red solid curves were obtained as described in Figure 7.

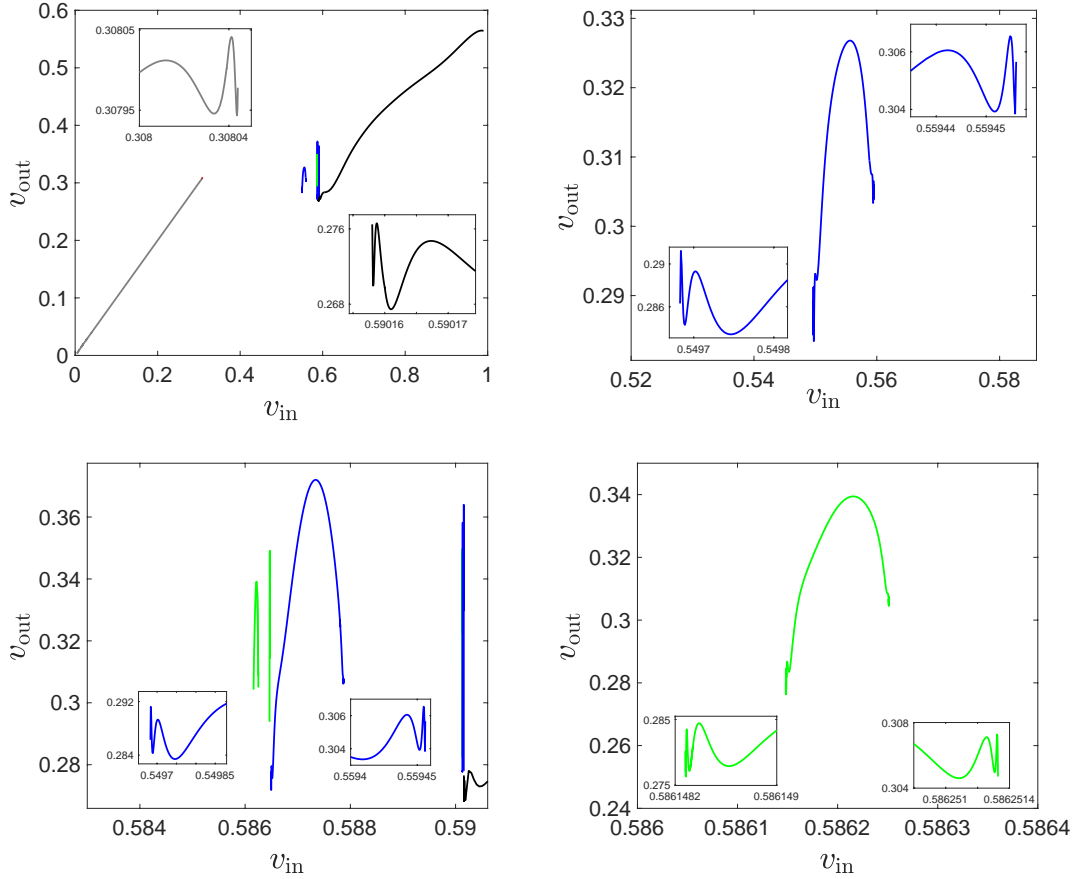


FIG. 9. The top left panel shows  $v_{out}$  vs  $v_{in}$  when  $\alpha = 1$  and  $\beta = 1$  with  $v_{2,crit} \approx 0.5902$ . The top right panel is the zoom-in about the first two-bounce curve. The bottom left panel is the zoom-in about the two three-bounce windows right before the critical velocity  $v_{2,crit}$ . The bottom right panel is the zoom in about the leftmost three-bounce window on the bottom left panel. In both top right and bottom panels, the tails and their oscillatory behaviors are shown. One-bounce windows in the figures are in solid black. Two-bounce windows are in blue and three bounce windows are in green. The gray solid line on the top left panel is when the kink-antikink repel each other elastically.

Having identified the critical point scaling relations, we now turn to a direct examination of the collision features

and associated multi-bounce windows. In Figure 9 we show  $v_{in} - v_{out}$  curves for  $\alpha = 1$  and  $\beta = 1$ . For fixed  $\beta = 1$  we know that the force law changes from the complex  $\lambda$  case to the real  $\lambda$  case at  $\alpha = 4$ , so we expect the case  $\alpha = 1$  to be somewhat similar to the pure biharmonic case of  $\alpha = 0$ . In the upper left panel of Figure 9 we see that the elastic collision region corresponds to  $0 < v_{in} < v_{1,crit} \approx 0.30805$  and the one-bounce region corresponds to  $v_{2,crit} \approx 0.5902 < v_{in} < 1$ . Note that we have chosen not to include  $v_{in}$  values greater than one. The region  $v_{1,crit} < v_{in} < v_{2,crit}$ , which corresponds to a bound state when  $\alpha = 0$ , is beginning to be populated by two and three bounce windows, a byproduct of the inclusion of the quadratic dispersion. The top right panel shows the first two-bounce window. The bottom left panel shows the next two-bounce window, with three-bounce windows appearing just to the left. The bottom right panel shows the first three-bounce window in more detail. All windows display the characteristic oscillations at the edges. Notice the important features of this case: on the one hand, the multi-bounce windows (which did *not* appear in the pure biharmonic case) are now present. On the other hand, they do not terminate as, e.g., in the case of the standard  $\phi^4$  model [6, 22], but rather have the oscillatory terminations (with progressively shorter periodicity) encountered previously in [30] for the pure biharmonic case. Moreover, we have encountered a feature also absent in the standard (pure)  $\phi^4$  case, namely higher-bounce windows appear only on one side (to the left) of the two bounce windows, while it is well-known [14] that they appear on both sides in the pure harmonic  $\phi^4$  problem.

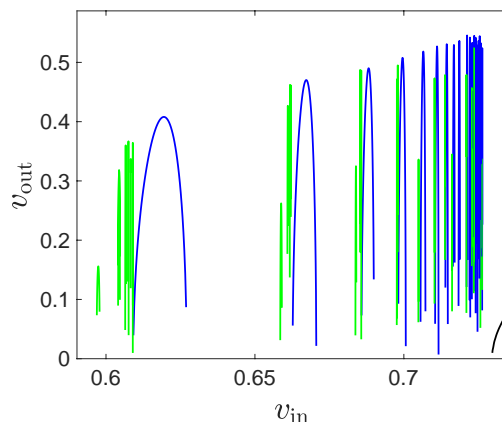


FIG. 10.  $v_{out}$  vs  $v_{in}$  when  $\alpha = 5$  and  $\beta = 1$  with  $v_c \approx 0.7295$ . The one-bounce window is in solid black. Two-bounce windows are in blue and three-bounce windows are in green.

In Figure 10 we show  $v_{in} - v_{out}$  curves for  $\alpha = 5$  and  $\beta = 1$ . For this case, since  $\alpha > 4$  we have  $\lambda$  real, and expect some similarity with the case of the pure  $\phi^4$  model ( $\beta = 0$ ). Indeed, the structure is similar to the fractal pattern we see in the  $\phi^4$  case, with three-bounce windows at the edges of the two bounce windows. However, we were not able to find three-bounce windows to the right of the two-bounce windows. These should, presumably, emerge as  $\alpha$  gets larger, or as  $\beta$  gets smaller. However, it is an open question requiring further systematic investigation how the self-similar (on both sides) picture of the pure  $\phi^4$  model arises.

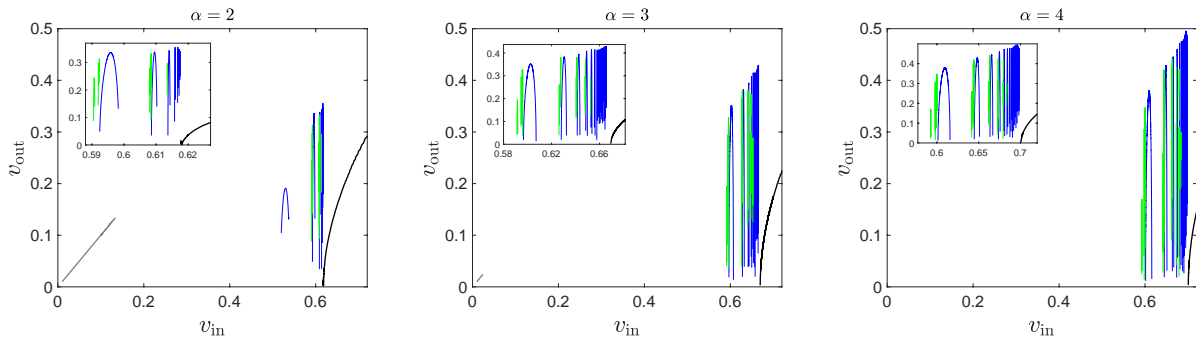


FIG. 11. Transition from dominant quartic progressively closer to dominant harmonic behavior, by changing  $\alpha$  from 2 (left) to 3 (middle) and finally the critical case of  $\alpha = 4$  (right panel).

We can begin to see how the system transitions from the  $\alpha = 0$ ,  $\beta = 1$  (pure quartic dispersion) case to the  $\alpha = 5$ ,

$\beta = 1$  (harmonic term dominant) case through some additional (less detailed)  $v_{in}$ - $v_{out}$  graphs; see, e.g., Figure 11. The first two-bounce window for  $\alpha = 2$  (left panel, main figure, and see also Figure 9 top left panel for  $\alpha = 1$ ) demonstrates a curious behavior. It appears (out of nowhere) at about  $\alpha = 0.711$ , persisting to about  $\alpha = 2.8$  where it disappears. This is why it arises in the left panel, but not the middle one. Similarly, notice how the transition shrinks progressively the size of the gray line interval of “no collision” for  $0 < v_{in} < v_{1,crit}$ . It can be seen that this interval eventually disappears for  $\alpha = 4$  in the right panel of the figure, again showcasing how the transition between the two regimes (biharmonic vs. harmonic) emerges.

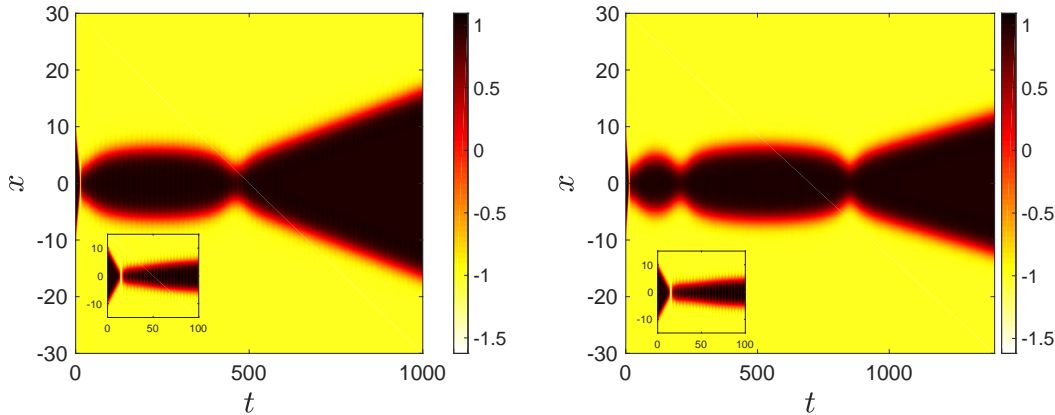


FIG. 12. Contour plots when  $\alpha = 2.05$  and  $\beta = 1$  with  $v_c \approx 0.6222$  for  $X(0) = 10$ . Left panel is when  $v_{in} = 0.622$  and right panel is when  $v_{in} = 0.621$ .

While in the discussion above, we have focused on features that transition the phenomenology between the two limits, it is important to realize that the wealth of the model considered here transcends that of solely the limit cases. For instance, Figure 12 illustrates a phenomenon not seen in either the pure biharmonic or the pure harmonic  $\phi^4$  case, with  $\alpha = 2.05$  and  $\beta = 1$ . What we see here is an initial interaction between kink and antikink, followed by separation of the solitons for a period of time, and then another approach of the pair. At this point one or more elastic collisions can occur, resulting in the appearance of multiple bounces. In the first panel of Figure 12 we see a “pseudo” two-bounce result, and in the second panel a pseudo three-bounce result. This can occur when the speed at which the kink and antikink approach each other for the second (or third) time is very small and therefore when we find ourselves in the small-speed reflection window of the complex eigenvalue case. In short, this is an unprecedented type of two-bounce since two-bounces cannot happen in the pure biharmonic case (where there is only bion formation and single bounce events [30]), but it can also not happen for pure harmonic  $\phi^4$  where the small speed reflection scenario is absent. This is yet another manifestation of the rich phenomenology of the model combining harmonic and biharmonic dispersion.

## VI. CONCLUSIONS & FUTURE CHALLENGES

In this work we have explored a model featuring the competition of a harmonic and biharmonic linear operator in a quadratic-quartic  $\phi^4$  model. We have argued that this model is of intrinsic mathematical interest due to the distinct implications of the different linear operators and also the unique features created by their interplay that neither of the “pure” (quadratic or quartic dispersion) models possesses. The harmonic part creates a saddle point in the spatial dynamics and hence leads to exponentially decaying waveforms. On the other hand, the biharmonic operator leads to complex eigenvalues and a spiral point in the corresponding spatial dynamics. Here, we have seen the interplay

of these two possibilities creating an effective competition between the two tendencies. We have observed that this competition leads to a critical point (with an intriguing behavior in its own right, i.e., a linearly modulated exponential) and on the two sides of this criticality either the biharmonic oscillatory effect or the harmonic exponential decay effect prevail respectively. This crucially affects the interactions between the kinks which we have also explicitly identified and corroborated by means of detailed comparison of both the single wave tails and of the two-coherent-structure interactions. We have also elucidated the extent to which this collective coordinate approach can be reliably used and illustrated its failure when the kinks get too close to each other. Additionally, we have examined the collisions, bounce and multi-bounce windows stemming from the kink interactions and have shown how the critical velocities and corresponding windows are modified as a function of the quadratic-quartic model parameters.

These findings will clearly have a significant bearing on the corresponding quadratic-quartic NLS model which is a natural possibility for future work, given the recent developments in pure quartic solitons [27, 28] and on optical media featuring quadratic and quartic dispersion [32]. This natural extension will have similar existence properties to the case considered herein, however the stability of the dark solitons of the latter problem is an interesting open question. Aside from this, both at the Klein-Gordon (real field-theoretic) level and at the NLS one, it will be interesting to generalize considerations to higher dimensional settings, where it is natural to expect, e.g., vortical and more generally topologically charged excitations. Corresponding studies are currently in progress and will be reported in future publications.

### ACKNOWLEDGMENTS

This material is based upon work supported by the US National Science Foundation under Grants PHY-1602994 and DMS-1809074 (P.G.K.).

- 
- [1] M.J. Ablowitz and H. Segur, *Solitons and the Inverse Scattering Transform*, SIAM (Philadelphia, 1981).
  - [2] M.J. Ablowitz and P.A. Clarkson, *Solitons, Nonlinear Evolution Equations and Inverse Scattering*, Cambridge University Press (Cambridge, 1991).
  - [3] P.G. Drazin, R.S. Johnson, *Solitons: An introduction*, Cambridge University Press (Cambridge, 1989).
  - [4] R. K. Dodd, J. C. Eilbeck, J. D. Gibbon, H. C. Morris, *Solitons and Nonlinear Wave Equations* (Academic Press, London, 1982).
  - [5] J. Cuevas, P.G. Kevrekidis, F.L. Williams (Eds.), *The sine-Gordon Model and its Applications: From Pendula and Josephson Junctions to Gravity and High Energy Physics*, Springer-Verlag, (Heidelberg, 2014).
  - [6] P.G. Kevrekidis and J. Cuevas-Maraver (Eds.), *A Dynamical Perspective on the  $\phi^4$  model*, Springer Nature (Heidelberg, 2019).
  - [7] A. E. Kudryavtsev, Solitonlike solutions for a Higgs scalar Field, Pis'ma Zh. Eksp. JETP Lett. **22**, 82 (1975).
  - [8] S. Aubry, Unified approach to interpretation of displace and order-disorder systems 2. Displace systems J. Chem. Phys. **64**, 3392 (1976).
  - [9] B.S. Getmanov, Bound States of Soliton in  $\phi_2^4$  Field-Theory Model, JETP Lett. **24**, 291 (1976).
  - [10] M. J. Ablowitz, M. D. Kruskal, and J. F. Ladik, Solitary Wave Collision, SIAM J. Appl. Math. **36**, 428 (1979).
  - [11] T. Sugiyama, Kink-antikink collisions in the two-dimensional  $\phi^4$  model, Prog. Theor. Phys., **61**, 1550 (1979).
  - [12] D.K. Campbell, J.S. Schonfeld, and C.A. Wingate, Resonance structure in kink-antikink interactions in  $\phi^4$  theory, Physica D, **9**, 1 (1983).
  - [13] T.I. Belova and A.E. Kudryavtsev, Solitons and their interactions in classical field theory, Phys. Usp., **40**, 359 (1997).
  - [14] P. Anninos, S. Oliveira, and R.A. Matzner, Fractal structure in the scalar  $\lambda(\phi^2 - 1)^2$  theory, Phys. Rev. D, **44**, 1147 (1991).
  - [15] R.H. Goodman and R. Haberman, Kink-antikink collisions in the  $\phi^4$  equation: The  $n$ -bounce resonance and the separatrix map, SIAM J. Appl. Dyn. Sys., **4**, 1105 (2005).
  - [16] R.H. Goodman, Chaotic scattering in solitary wave interactions: A singular iterated-map description, Chaos, **18**, 023113 (2008).
  - [17] H. Weigel, Kink-antikink scattering in  $\phi^4$  and  $\phi^6$  models, J. Phys. Conf. Ser., **482**, 012045 (2014).
  - [18] I. Takiy and H. Weigel, Collective coordinates in one-dimensional soliton models revisited, Phys. Rev. D, **94**, 085008 (2016).
  - [19] N. S. Manton, K. Oleś, T. Romańczukiewicz, A. Wereszczyński, Kink Moduli Spaces – Collective Coordinates Reconsidered, arXiv:2008.01026.
  - [20] C.F.S. Pereira, G. Luchini, T. Tassis, and C.P. Constantinidis, Some novel considerations about the collective coordinates approximation for the scattering of  $\phi^4$  kinks, arXiv:2004.00571.
  - [21] D. Bazeia, Adalberto R. Gomes, Fabiano C. Simas, Semi-compactness and multiple oscillating pulses in kink scattering, arXiv:2011.11157.
  - [22] M. Lizunova, J. van Wezel, An introduction to kinks in  $\phi^4$ -theory, arXiv:2009.00355.

- [23] S. Levandosky, Stability and instability of fourth order solitary waves, *J. Dynam. Diff. Eqs.*, **10**, 151 (1998).
- [24] A.R. Champneys, P.J. McKenna, and P.A. Zegeling, Solitary waves in nonlinear beam equations: stability, fission and fusion, *Nonlinear Dynamics*, **21**, 31 (2000).
- [25] Y. Chen and P.J. McKenna, Traveling waves in a nonlinearly suspended beam: theoretical results and numerical observations, *J. Diff. Eqs.*, **136**, 325 (1997).
- [26] P. Karageorgis and P.J. McKenna, The existence of ground states for fourth-order wave equations, *Nonlinear Anal.*, **73**, 367 (2010).
- [27] A. Blanco-Redondo, C. Martijn de Sterke, J.E. Sipe, T.F. Krauss, B.J. Eggleton, and C. Husko, Pure-quartic solitons, *Nature Comms.*, **7**, 10427 (2016).
- [28] A.F.J. Runge, D.D. Hudson, K.K.K. Tam, C.M. de Sterke, A. Blanco-Redondo, The pure quartic soliton laser *Nat. Photonics* **14**, 492 (2020).
- [29] A. Demirkaya and M. Stanislavova, Numerical results on existence and stability of standing and traveling waves for the fourth order beam equation, *Discrete Contin. Dyn. Syst. B*, **24**, 197 (2019).
- [30] R. Decker, A. Demirkaya, P.G. Kevrekidis, D. Iglesias, J. Severino, and Y. Shavit, Kink dynamics in a nonlinear beam model, arXiv:2001.06973.
- [31] I. Posukhovskiy and A. Stefanov, On the normalized ground states for the Kawahara equation and a fourth order NLS, *Discr. Cont. Dyn. Sys. A* **40**. 4131-4162 (2020).
- [32] K.K.K. Tam, T.J. Alexander, A. Blanco-Redondo, and C.M. de Sterke, Generalized dispersion Kerr solitons, *Phys. Rev. A* , **101**, 043822 (2020).
- [33] R. J. Decker, A. Demirkaya, N. S. Manton and P. G. Kevrekidis, Kink-antikink interaction forces and bound states in a biharmonic  $\phi^4$  model, *J.Phys. A*, **53**, 37 (2020).
- [34] N.S. Manton, An effective Lagrangian for solitons, *Nucl. Phys. B*, **150**, 397 (1979).
- [35] I.C. Christov, R. Decker, A. Demirkaya, P.G. Kevrekidis, and V.A. Gani, Long range interactions of kinks, *Phys. Rev. D*, **99**, 016010, (2019).